

## A study of acoustic propagation from a large bolide in the atmosphere with a dense seismic network

Michael A. H. Hedlin,<sup>1</sup> Doug Drob,<sup>2</sup> Kris Walker,<sup>1</sup> and Catherine de Groot-Hedlin<sup>1</sup>

Received 26 April 2010; revised 11 July 2010; accepted 5 August 2010; published 17 November 2010.

[1] A large meteor entered the atmosphere above northeastern Oregon on 19 February 2008 at 530 PST. Several hundreds of broadband seismic stations in the U.S. Pacific Northwest recorded acoustic-to-seismic coupled signals from this event. The travel times of the first arriving energy are consistent with a terminal explosion source model, suggesting that the large size of the explosion masked any signals associated with a continuous line source along its supersonic trajectory. Several infrasound arrays in North America also recorded this event. Both the seismic and infrasound data have been used to locate the explosion in 3-D space and time. Climatological atmospheric velocity models predict that infrasound signals from sources that occur at mid-northern latitudes in winter are usually ducted to the east due to eastward zonal winds. In this paper, we analyze travel time picks and use 3-D ray tracing to generate synthetic travel times based on various atmospheric models to show that the seismic network data instead reveal a predominant westward propagation direction. A sudden stratospheric warming event that reversed the zonal wind flow explains this westward propagation. The seismic data illuminate in unprecedented spatial detail the range and azimuthal definition of shadow zones out to a range of 500 km, suggesting that dense seismic networks can be used to study infrasound propagation at spatial resolutions that exceed that which can be done with only a handful of globally distributed infrasound arrays.

**Citation:** Hedlin, M. A. H., D. Drob, K. Walker, and C. de Groot-Hedlin (2010), A study of acoustic propagation from a large bolide in the atmosphere with a dense seismic network, *J. Geophys. Res.*, 115, B11312, doi:10.1029/2010JB007669.

### 1. Introduction

[2] Infrasound is a subaudible (<20 Hz) acoustic energy in the atmosphere that is generated by a broad suite of natural phenomena and man-made sources [Bedard and Georges, 2000]. We learned of infrasound in 1883 as very long period infrasound waves from the cataclysmic eruption of Krakatoa that circled the Earth at least 7 times [Symons, 1888]. Higher-frequency infrasound and audible signals from this event were detected to a range of several thousands of kilometers [Symons, 1888]. In addition to volcanic eruptions, any phenomenon in the atmosphere or the shallow Earth that can compress a large volume of air is a potential infrasound source. Many natural sources (such as bolides, earthquakes, large avalanches, rockfalls, and large storms) in addition to man-made sources (such as nuclear and chemical explosions, rocket launches, supersonic aircraft) generate infrasound [Bass et al., 2006; Hedlin, 2006; Le Pichon et al., 2002a, 2002b; Mikumo, 1968].

[3] Because of its low frequency, infrasound propagates with relatively little energy loss and can be used to detect and probe the underlying physics of these sources at ranges of several hundreds to several thousands of kilometers. The atmosphere is acoustically anisotropic. Infrasound is ducted by temperature increases at higher altitudes (because acoustic velocity is directly proportional to the square root of absolute air temperature) but also by favorable winds in the stratosphere and the troposphere [Georges and Young, 1972; Georges and Beasley, 1977; de Groot-Hedlin, 2008; de Groot-Hedlin et al., 2010]. Infrasound can also be ducted within the higher-altitude thermosphere due to its high temperature but is heavily attenuated due to the low molecular density in this layer [Sutherland and Bass, 2004].

[4] Infrasound is used for international nuclear test ban treaty monitoring. A 60-station global network of 1–3 km aperture infrasound arrays capable of locating a 1 kT nuclear explosion in the atmosphere is being constructed as part of the International Monitoring System (IMS), which will be used to monitor compliance with the Comprehensive Nuclear-Test-Ban Treaty (CTBT) [Le Pichon et al., 2009]. Including research arrays, there are on the order of 100 infrasound arrays operating worldwide as of 2010. Most infrasound studies employ analysis of data collected by such sparsely located infrasound arrays. For example, infrasound has been used to probe the structure of the atmosphere, in particular at altitudes not constrained well by ground-based systems

<sup>1</sup>Laboratory for Atmospheric Acoustics, Institute of Geophysics and Planetary Physics, Scripps Institution of Oceanography, University of California, San Diego, La Jolla, California, USA.

<sup>2</sup>Upper Atmospheric Modeling Section, Naval Research Laboratory, Washington, D. C., USA.

or satellites [e.g., *Le Pichon et al.*, 2002a; *Garces et al.*, 2004].

[5] The performance of the IMS infrasound array network in detecting explosions has been assessed [*Le Pichon et al.*, 2009; *Green and Bowers*, 2009]. Several studies have shown the utility of infrasound stations for locating events [e.g., *Brown et al.*, 2002; *Arrowsmith et al.*, 2008]. Although the density of infrasound stations is without precedent, the network is still relatively sparse compared to synoptic and small-scale changes of the atmosphere (for a review, see *de Groot-Hedlin et al.* [2010] and *Norris et al.* [2010]). The atmosphere changes continuously at both fine scales (e.g., gravity waves) [*Gibson et al.*, 2009; *Norris et al.*, 2010] and large scales due to the temporal evolution of planetary waves and migrating tides [*de Groot-Hedlin et al.*, 2010; *Drob et al.*, 2010b]. Therefore, for a series of identical sources at the same location separated by hours or days and recorded by the same infrasound stations, the waveforms would not repeat from one source to the next but may vary significantly [e.g., *Herrin et al.*, 2008]. In general, long-range propagation through the stratosphere primarily depends on the behavior of the east-west zonal stratospheric wind jet. At midlatitudes, these winds reverse twice per year. The stratospheric duct depends critically on the zonal winds, with little energy expected at the ground at points upwind of the source [*Georges and Young*, 1972]. Our ability to model this time-varying structure has advanced [e.g., *Drob et al.*, 2003, 2008, 2010a], as has our ability to synthesize infrasound propagation through it [e.g., *Millet et al.*, 2007; *de Groot Hedlin*, 2008].

[6] It is well known that infrasound waves from atmospheric sources load the Earth's surface and couple to seismic energy often above background seismic noise [e.g., *Kanamori et al.*, 1991; *Edwards*, 2003; *Langston*, 2004; *Cochran and Shearer*, 2006; *de Groot-Hedlin et al.*, 2008; *Rogers et al.*, 2008]. While it is also well known that the underlying geology beneath each seismic station has a great influence on both the amplitude and character of acoustic-to-seismic coupled signals, the onset times for the arriving energy are accurately preserved during the acoustic-to-seismic energy conversion. Therefore, seismic network studies of large acoustic events using onset times only require the initial assumption that the signal-to-noise ratio is adequate for picking, which can be validated later with infrasound propagation modeling. Seismic networks record signals from large atmospheric sources and sample properties of the infrasound wavefield at a considerably higher spatial density than is possible with existing infrasound arrays. Although the station density is highly variable, there are several thousands of broadband seismometers in use worldwide. In heavily instrumented areas, travel times from first arrivals can be used to accurately locate the infrasound source in 3-D space and time [*Edwards*, 2003]. Once the source is located, the travel times of multipathed arrivals can be used to study infrasound propagation at a nearly continuous function of range and azimuth from the source to the ground, a task that would be impossible with only a few infrasound arrays spaced several thousands of kilometers apart.

[7] In this paper, we present a study of a large bolide that exploded above and in the vicinity of several hundreds of broadband seismic stations in the U.S. Pacific Northwest on 19 February 2008. The seismic network recorded several hundreds of acoustic-to-seismic coupled signals due to the

event. Bootstrap resampling procedures place the terminal burst in northeast Oregon in the middle stratosphere. We defer additional details on the source location to *Walker et al.* [2010]. We show that the dense seismic network data reveal several branches of infrasound propagation from the elevated source to the ground predominantly to the west of the event. This is atypical; empirical atmospheric velocity models predict that sources that occur at mid-northern latitudes in winter are usually detected to the east due to eastward zonal winds. Using 3-D ray tracing through a composite atmospheric model, we show that the event occurred during a major sudden stratospheric warming event [e.g., *Manney et al.*, 2008; *Wang and Alexander*, 2009; *Evers and Siegmund*, 2009] that reversed zonal wind flow favoring stratospheric ducting to the west.

## 2. Study Area

[8] In terms of infrasound propagation, the U.S. Pacific Northwest is located at a latitude where eastward stratospheric winds generally occur during the Northern Hemisphere winter. The result is preferential ducting of infrasound to the east [e.g., *Georges and Beasley*, 1977; *Le Pichon et al.*, 2009]. During the summer months, the stratospheric winds reverse, resulting in predominant westward ducting. In addition, the strong polar tropospheric jet stream meanders over the northwest United States, resulting in variable eastward tropospheric ducting. But the Northern Hemisphere winter-time general circulation is much more variable as compared to the hemispherically stable summertime conditions. The seasonal variability of infrasound propagation in the region over a 5 year time series was recently investigated theoretically by *Drob et al.* [2010b]. Typically minor sudden stratospheric warming events, where the stratospheric zonal wind slow but do not reverse, occur several times each winter. Major sudden stratospheric warming events, where the polar stratospheric vortex is completely disrupted with the zonal winds reversing directions for periods of several weeks over a broad range of longitudes, typically occur about every other year.

## 3. Seismic and Video Observations

[9] The USArray and regional seismic networks in the Pacific Northwest area of the United States provided data for this study. At the time of the event, the USArray extended north-south across the continental United States and east-west at ~700 km from the bolide event in each direction (Figure 1). The bolide explosion was surrounded by ~500 seismic stations of the USArray and regional networks (Figure 2, white and colored circles). Two temporary PASCALL seismic deployments were in progress at the time of the bolide. The Wallowa Flexible Array network, by Gene Humphries of the University of Oregon, comprised over 10 broadband seismometers. The High Lava Plains Seismic Experiment, led by Matt Fouch of the University of Arizona and David James of the Carnegie Institution of Washington, involved a dense network of over 90 broadband seismometers. Seismic recordings made at these arrays have been used to investigate crustal and upper mantle structures within Oregon [*Long et al.*, 2009; *Scarberry et al.*, 2009; *Warren et al.*, 2008]. The IMS infrasound array I56US was

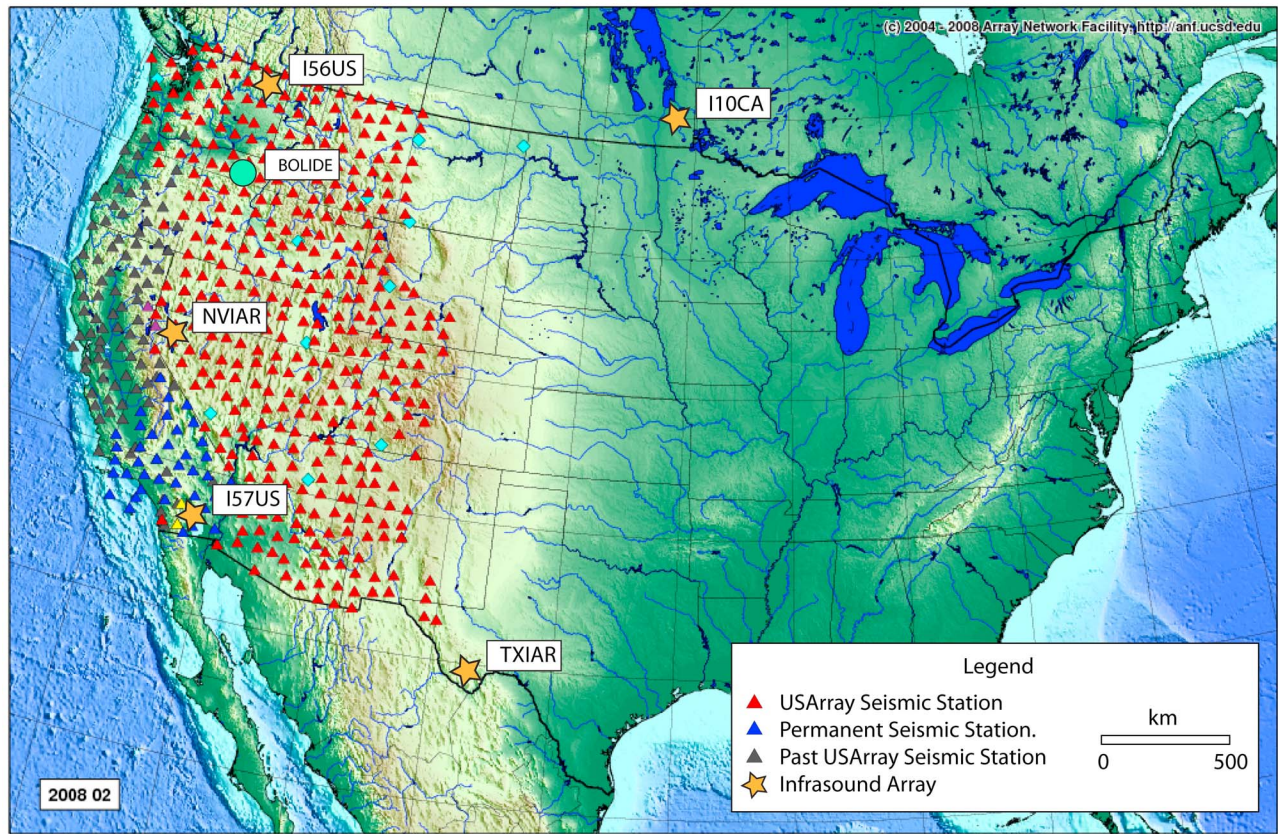


**Figure 1.** Cumulative sum of USArray stations between 2004 and February 2008 and infrasound arrays that recorded data during the same time span. The average seismic station deployment is 2 years. Red and blue stations are those that were active at the time of the Oregon bolide explosion. The background image was downloaded from the Earthscope ANF Web site ([http://anf.ucsd.edu/stations/deployment\\_history.php](http://anf.ucsd.edu/stations/deployment_history.php)).

also located 300 km from the explosion. Here our interest is only in acoustic signals recorded at the seismic stations. We analyze only vertical component data near 1 Hz.

[10] Several video cameras recorded the terminal explosion (Figure 2, black triangles). Azimuths and uncertainties from three video cameras to the center of the explosion were estimated using objects in the foreground. An all-sky camera in West Kelowna, British Columbia, provided a single azimuth. The video cameras and the all-sky camera place the terminal burst above the Blue Mountains in NE Oregon. An all-sky camera in Calgary, Alberta, was synced to universal time and provided the time of the final burst to within 1 s. Additional details of the video constraints on the source location are discussed by Walker *et al.* [2010].

#### 4. Analysis

##### 4.1. Observations

[11] The bolide was located in 2-D space and time by reverse time migration (RTM) of envelope functions of 1–5 Hz band-pass-filtered vertical component USArray seismic data [Walker *et al.*, 2010]. The uncertainties were estimated via a bootstrap technique. The source time and altitude were estimated via a separate grid search using 3-D ray tracing with an European Centre for Medium-Range Weather Forecasts

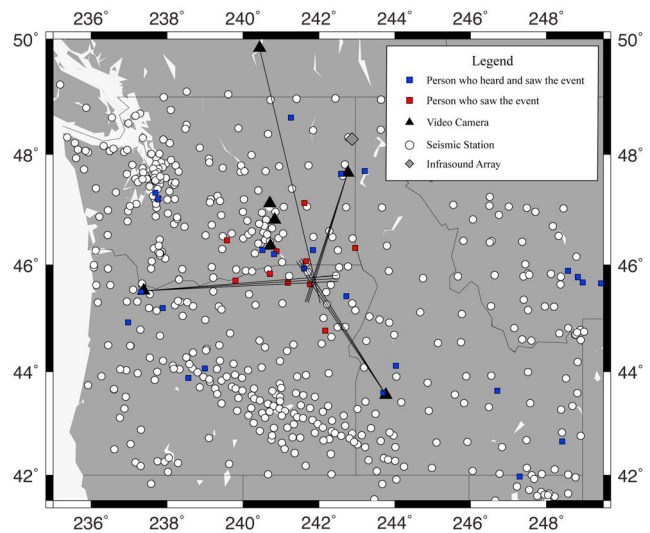


**Figure 2.** Map of study area. The lines indicate azimuths (with uncertainty limits where available) from the video cameras to the terminal flash.

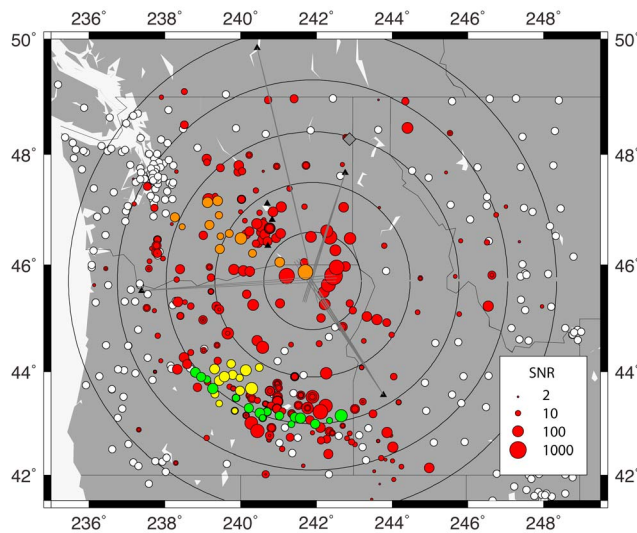


**Figure 3.** Stations that did not record a signal shortly after the terminal burst are represented by the small white disks. Stations that did record a signal are colored with the symbol size scaled by the ratio of signal-to-noise in the frequency band from 0.8 to 3.0 Hz (as shown in the legend). Data from the orange, yellow, and green stations are shown in Figures 5a, 5b, and 5c, respectively. Most stations that recorded this event are located to the west. The expanding set of rings mark intervals of 100 km from the source location. The black triangles are video cameras, and the diamond is the infrasound array I56US (as explained in the caption to Figure 2).

(ECMWF) model. The reverse time migration approach does not require an assumption about the source model or manual arrival picking. The RTM results suggest that the dominant signals observed by the seismic networks result from a point source. Back azimuths from several video cameras that recorded the bolide point to a terminal flash of light 2 km from the seismic source location. These results suggest that the terminal burst of the bolide created a point source of acoustic energy that was sampled by the seismic networks and that the seismic source location is accurate.

[12] It is well known that infrasound can travel through the atmosphere from one point to another along multiple paths. After the bolide source location was determined, the seismic waveforms were passband filtered to a frequency band spanning 1 Hz, because the bulk of the signals had a frequency content between 0.8 and 3.0 Hz. In some cases, however, energy was observed above or below these limits, and different filters were used during the picking stage to produce the most accurate estimate of the signal onset time. We manually picked the onset times of energy packets in station time windows assuming a linear moveout velocity range of 275–325 m/s. Some sensors recorded at least one clear acoustic-to-seismic coupled signal within these predicted time windows, while others did not. The colored symbols shown in Figure 3 recorded some signal after the explosion and are scaled by the ratio of the signal-to-presignal noise amplitude. The uncolored and unscaled symbols in Figures 2 and 3 represent stations that did not record a signal above noise. Although Figure 3 only shows a signal

being detected out to 500 km distance, additional analysis of seismic data from the entire USArray shows that a bolide signal was consistently recorded out to a range of 800 km [Walker *et al.*, 2010].

[13] An obvious pattern exists in the travel time picks; there are many more stations that detected a bolide signal to the south and west of the epicenter than to the north and east (Figure 3). Furthermore, within the first 100 km, the maximum signal-to-noise ratio (SNR) for each station is generally larger to the north and east. At ranges greater than 100 km, the SNR is generally greater to the south and west.

[14] The signal-to-noise ratios rather than absolute amplitudes are shown in Figure 3 because different geologic site conditions are known to give rise to varying acoustic-to-seismic transmission factors [e.g., Langston, 2004]. The absolute seismic noise levels are shown in Figure 4. To define the noise amplitude, we calculated the mean value of the envelope function of the 0.8–3 Hz band-pass-filtered data for a 100 s long noise window centered at 1315 UTC. The seismic noise is about 15 dB greater to the northwest than to the east. This indicates that the patterns shown in Figure 3 are likely due to propagation and not a result of variation in background seismic noise level.

[15] The orange symbols shown in Figure 3 to the west of the source represent stations selected for the record section shown in Figure 5a. Recordings from the stations highlighted in yellow are shown in Figure 5b; green stations are shown in Figure 5c. The waveforms are all normalized by their respective maximum values for plotting purposes.

[16] The first arriving energy for a profile to the northwest shows linear moveout for ranges past 100 km (Figure 5a). A continuous line source model was found to explain the acoustic-to-seismic coupled signals recorded by seismometers in Southern California created by the supersonic reentry of the Shuttle Atlantis [de Groot-Hedlin *et al.*, 2008]. In contrast to that model, the travel times for the first arriving energy of this bolide are shown by Walker *et al.* [2010] to be due to a terminal explosion at the same latitude and longitude obtained by the reverse time migration result but with a stratospheric elevation.

[17] The record sections in Figure 5 show four different traveltimes branches, which are identified by their celerity. Celerity is defined as source-receiver offset divided by observed travel time. The record section in Figure 5a shows clearly two traveltimes branches along a single azimuth to the northwest. The first branch extends from the source region to past 250 km. The second arriving branch begins at 200 km and extends past 300 km. The first branch appears at a progressively higher celerity with increasing range (due to the hyperbolic moveout associated with the source altitude), reaching ~315 m/s past a range of 200 km. The celerity of the slower branch also increases with increasing range, reaching 295 m/s at a range of 300 km. The waveform packets associated with these branches are about 15 s long.

[18] The record section to the southwest of the event is quite different (Figure 5b). Two branches are observed at celerities of about ~315 m/s. The second arriving branch appears at a range of ~230 km. The waveform packets defining both of these branches are ~30 s long and are the same branches observed in Figure 5a. However, a new much slower branch is observed with a celerity ranging from 220

0.8–3 Hz BHZ Noise at 2008/02/19 1315 UTC

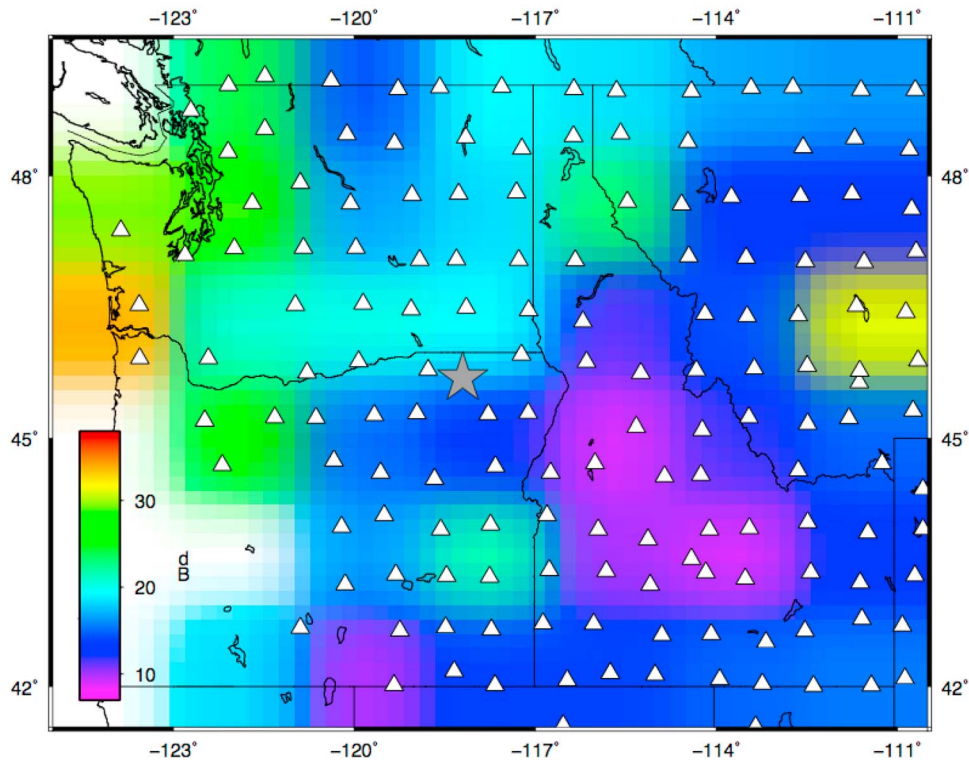


**Figure 4.** Vertical component seismic background noise in the 0.8–3 Hz band 15 min before the bolide entered the atmosphere. The color scale is in units of dB with respect to 1 nm/s. Seismic noise was about 15 dB greater in the northwest than in the southeast.

to 250 m/s. The waveforms comprising this slow branch are more impulsive and have a duration of only  $\sim 5$  s.

[19] In Figure 5c, we plot data from stations at a range of 300 km and between azimuths of  $210^\circ$ – $235^\circ$  from the source. All three branches already shown in Figure 5b are seen; however, the fastest branch near 310 m/s gradually fades from view with decreasing azimuth. The second branch fades more rapidly with decreasing azimuth. A new, third fastest branch emerges for azimuths less than  $210^\circ$ . The slowest branch near 250 m/s is seen between  $178^\circ$  and  $230^\circ$ .

[20] The signal character of each branch appears to be relatively independent of range, other than the amplitude changes relative to noise noted earlier. This suggests a lack of a significant site effect at any of the stations or, less likely, suggests very similar site effects at all stations. The steady moveout of the signals with increasing range from the source clearly indicates that all signals are from the same source and that the sound produced by the bolide has reached the receivers along multiple paths.

[21] There are two metrics by which to identify traveltime branches: apparent phase velocity and celerity. For ducted and tropospheric phases, traveltime branches will converge to a constant apparent phase velocity and celerity when the ratio of the range to source altitude is much greater than 1. For reflections, this is not the case, since the apparent phase velocity will consistently vary with range. Although apparent phase velocity is a relatively easy metric to utilize because it does not rely on a priori knowledge of the source location

and time, its measurement generally requires an infrasound array. The celerities of all the observed traveltime branches at all azimuths out to 500 km range are summarized in Figure 6. Because of the picking technique employed, some of the picked “signals” may have been local noise bursts unrelated to the event, which would appear as “clutter.” Signals that are well above noise and lie on celerity branches can be confidently associated with acoustic-to-seismic coupled signals from the bolide explosion.

[22] We observe a fast branch (labeled branch 1 in Figure 6) extending from the source region to  $\sim 350$  km (Figure 7a). The signals observed at distances  $< 100$  km occur at all azimuths from the source. The more distant signals on this branch are predominantly recorded to the southwest, west, and northwest of the event. This is the first arriving branch seen in Figures 5a–5c. The second fastest branch (labeled branch 2 in Figure 6) lies at distances from  $\sim 200$  to  $\sim 350$  km with virtually all stations located to the southwest, west, and northwest of the source (Figure 7b). This is the second arriving branch seen in Figures 5a–5c. A few arrivals are detected at stations from 100 to 200 km to the southeast of the event. The third branch (Figure 6, branch 3) extends from 200 to nearly 400 km from the event and lies at celerities from 260 to 295 m/s (Figures 5c and 7c). The fourth, slowest branch (Figure 6, branch 4) lies just to the southwest of the event at distances from 200 to 350 km and celerities from 225 to 305 m/s (Figure 7d). This is the weaker, late arriving branch seen in Figures 5b and 5c.

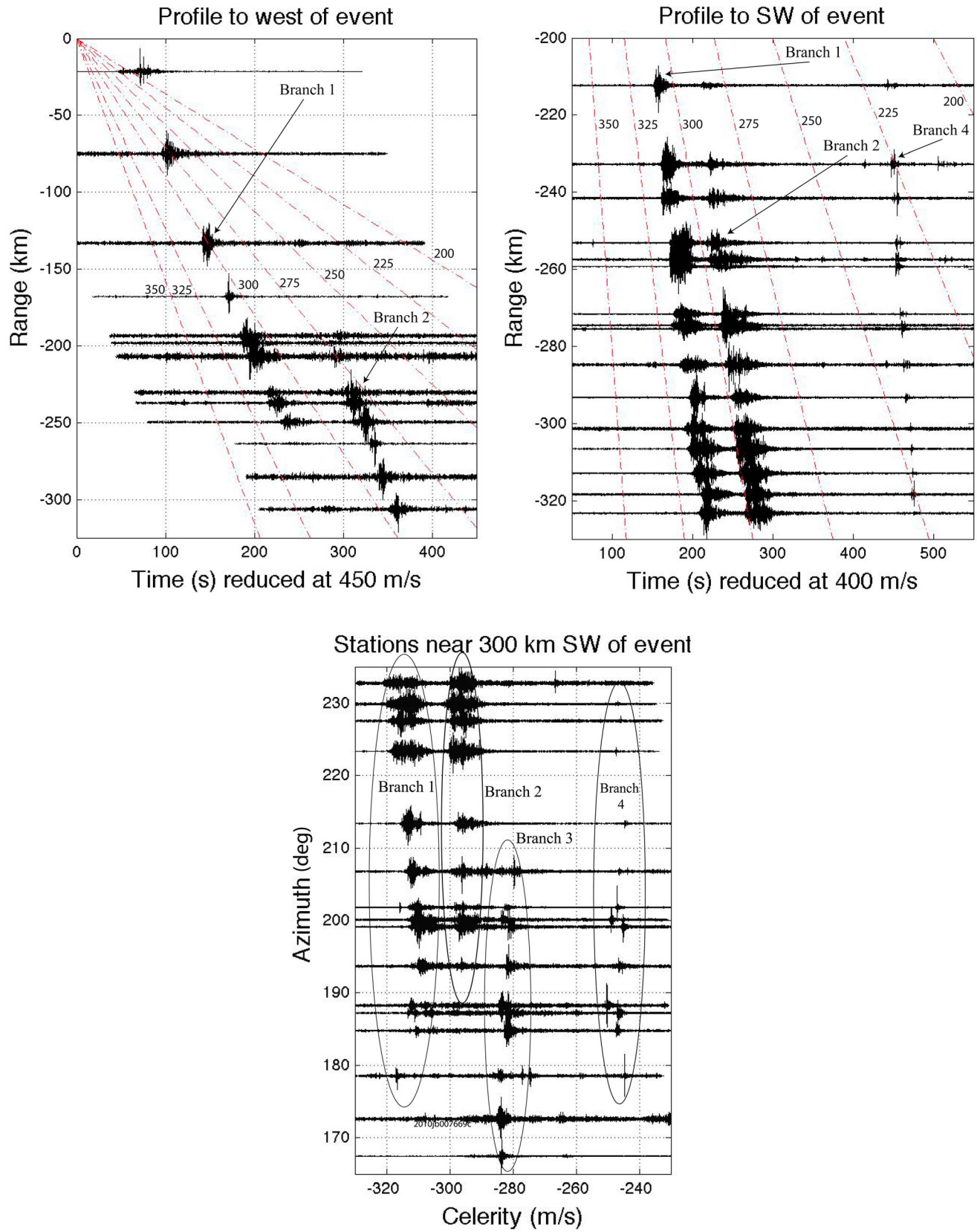
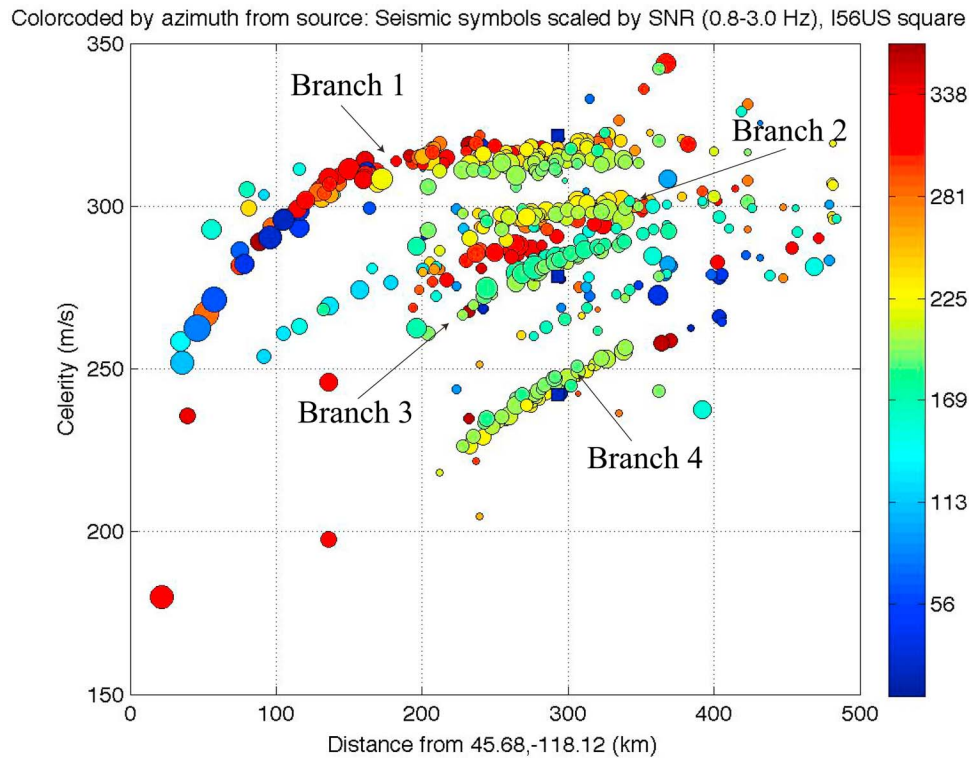


Figure 5



**Figure 6.** Celerity of all seismic and infrasound signals within 500 km range showing the different traveltime branches. The symbols are color coded by azimuth from the source. The symbols are also scaled by the maximum signal-to-noise ratio (same as in Figure 3).

[23] Although the combined seismic networks provide much greater coverage of the infrasound wavefield than is provided by the global infrasound array network, the seismic coverage here is uneven (because of different research objectives), with the densest collection of stations to the south of the source. It is possible that some of the branches (especially branches 3 and 4) land on a somewhat larger area than implied by the seismic data. Specifically, the coverage of these branches is excellent as a function of azimuth from the source, but coverage is more uneven with range. In just considering the azimuthal variation, both Figures 5c and 7 illuminate shadow zones, where infrasound does not reach due to specific variations in ambient sound speed and wind between the source and receiver.

[24] Infrasound signals from the bolide were recorded by I56US, an IMS infrasound array with a 2 km aperture located in Newport, Washington. These signals are discussed in greater detail in Walker *et al.* [2010]. Three infrasound signals were observed over a 6 min period. The great circle azimuth from the array to the seismic location is  $196^\circ$ . Array

processing indicates that all signals have back azimuths of  $192^\circ$ – $196^\circ$ . The observed celerities of the arrivals are 321, 278, and 242 m/s, which are consistent with those obtained by the seismic analysis (e.g., Figure 6).

#### 4.2. Ray Modeling

[25] The travel times of the observed arrivals were predicted using ray tracing in a fully 3-D, range-dependent environment [Drob *et al.*, 2003] derived from the  $0.5^\circ \times 0.5^\circ$ , 91-level resolution European Centre for Medium-Range Weather Forecasts (ECMWF) analysis products [Persson and Grazzini, 2007] up to 75 km and the HWM07/MSISE-00 empirical climatologies [Drob *et al.*, 2008; Picone *et al.*, 2002] above. The acoustic ray tracing is performed with the Eikonal ray tracing equations of Gossard and Hooke [1976], ignoring vertical wind and terms involving neutral buoyancy. The calculations also account for surface reflections from uneven topography given by the NOAA GLOBE 30" digital terrain model [Hastings *et al.*, 1999]. A total of 125,664 uniformly distributed rays were integrated

**Figure 5.** (a) Distance-time plot of recorded vertical component seismic waveforms in the 0.8–3.0 Hz band for stations to the northwest of the bolide explosion. Reduced time in the record section assumes the ground level source at  $45.719^\circ\text{N}$ ,  $118.122^\circ\text{W}$ , and 133029 UT. The red dashed lines indicate constant celerity (source-receiver offset divided by travel time, in m/s). The stations used in Figure 5a are shown in orange in Figure 3. (b) Distance-time plot of recorded vertical component seismic waveforms in the 0.8–3.0 Hz band for stations to the southwest of the bolide explosion. Reduced time in the record section assumes the ground level source at  $45.719^\circ\text{N}$ ,  $118.122^\circ\text{W}$ , and 133029 UT. The red dashed lines indicate constant celerity (source-receiver offset divided by travel time, in m/s). The stations used in Figure 5b are shown in yellow in Figure 3. (c) Azimuth-celerity plot of vertical component seismic waveforms in the 2.0–8.0 Hz band for stations to the southwest of the bolide explosion at a range of 290–310 km (green symbols in Figure 3). Four different interpreted traveltime branches are identified.

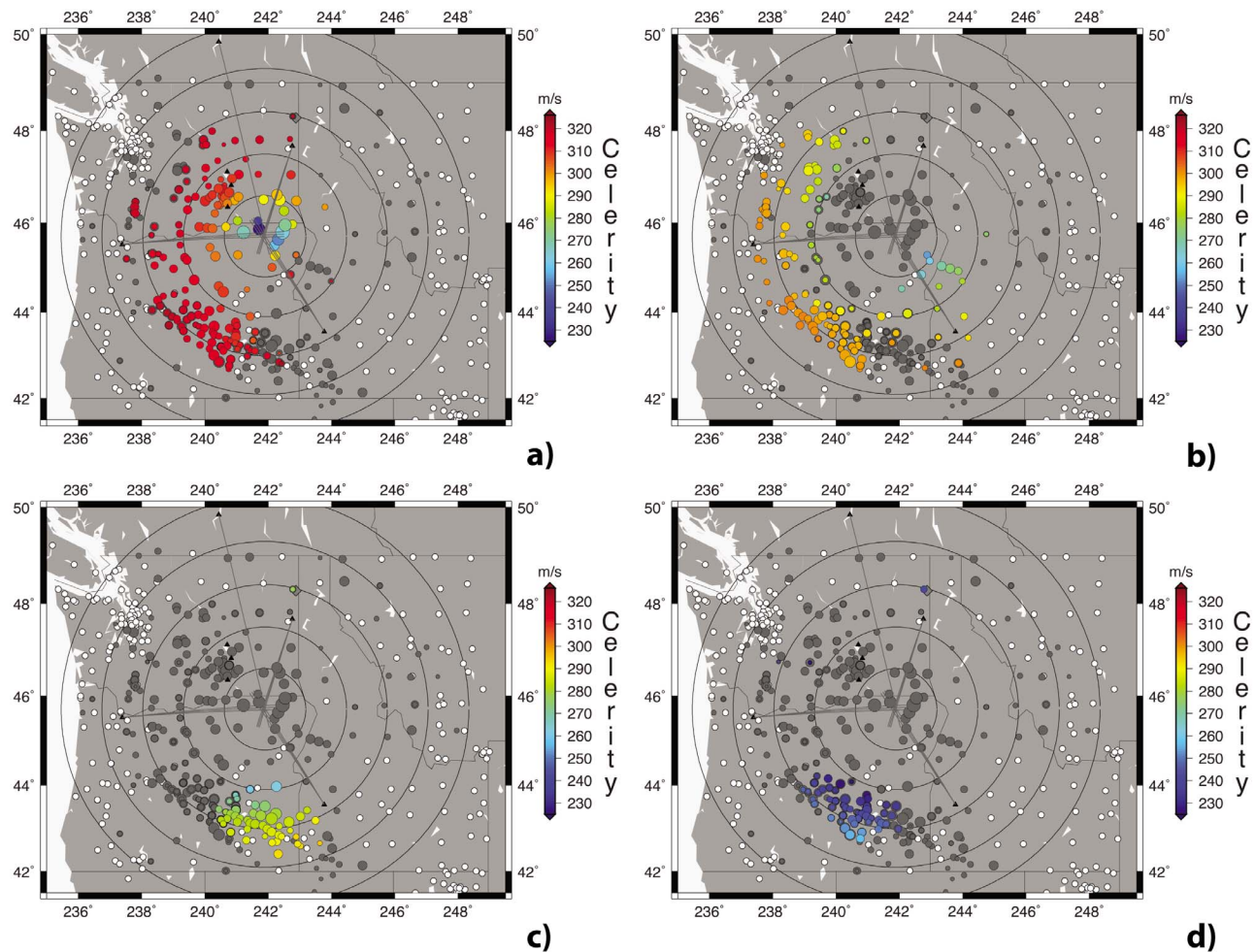


**Figure 7.** Observed traveltime branches. The ray landing points for branches 1–4 are shown in Figures 7a–7d, respectively. (a) The signals as  $d$  within 100 km of the source and a combination of  $dW_n$ ,  $uS$ , and  $uSW_n$  at greater distances (i.e., the branch is an amalgamation of more than one propagation path). (b) Landing points of the branch we interpret as  $dS$ . (c) Landing points of branch 3. (d) Landing points of branch 4, which we interpret as  $uT$ . The terms used in this caption are defined in Appendix A.

forward in time from a spherical point source at the estimated source location 27 km above the ground. When a downward propagating ray made contact with the surface, the location and time of that contact was recorded. To illustrate the nature of the calculations, computed paths for those rays that encounter the ground toward an azimuth of  $210^\circ$  are shown in Figure 8. For plotting purposes, range independence of the background atmosphere was assumed and topography was temporally ignored.

[26] The celerities of the predicted rays that reach the ground are shown in Figure 9. Figures 8 and 9 show that infrasound rays are predicted to group onto a number of well-defined branches, as seen in the recorded data. The raypaths range in complexity from simple propagation directly to the ground to complex propagation involving a number of free-surface bounces. Considering the observed complexity of some of the raypaths and a need to easily reference infrasound phases that propagate along all possible raypaths that eventually reach the ground, we propose a new nomenclature for infrasound propagation (Appendix A).

[27] First, at ranges less than 100 km from the source, the propagation is simply down to the ground, i.e., branch  $d$  following the new nomenclature. At ranges beyond 100 km, the rays are tropospherically ducted after propagating directly to the ground from the source ( $dW_n$ ). These modes extending into a long tail of constant celerity ( $\sim 320$  m/s) for that energy trapped near the surface out to ranges greater than 300 km (Figures 8 and 9). Starting at distances of about 150 km, the rays propagated up from the source and were ducted back to the ground from within the stratosphere ( $uS$ ). These rays have a similar celerity such that the  $dW_n$  and  $uS$  branch coalesce in the record sections (Figure 5) making it difficult to delineate where the  $d$  arrivals end and the  $uS$  arrivals begin. Although the  $d$  and  $dW_n$  rays are predicted at all azimuths, the stratospherically ducted rays land to the west of the source due to zonal winds directed from east to west. Again, like the  $dW_n$  rays, the  $uS$  rays can become trapped near the surface as the result of range dependence and topography ( $uSW_n$ ). The next branch of stratospheric rays that are ducted in the stratosphere after a ground bounce

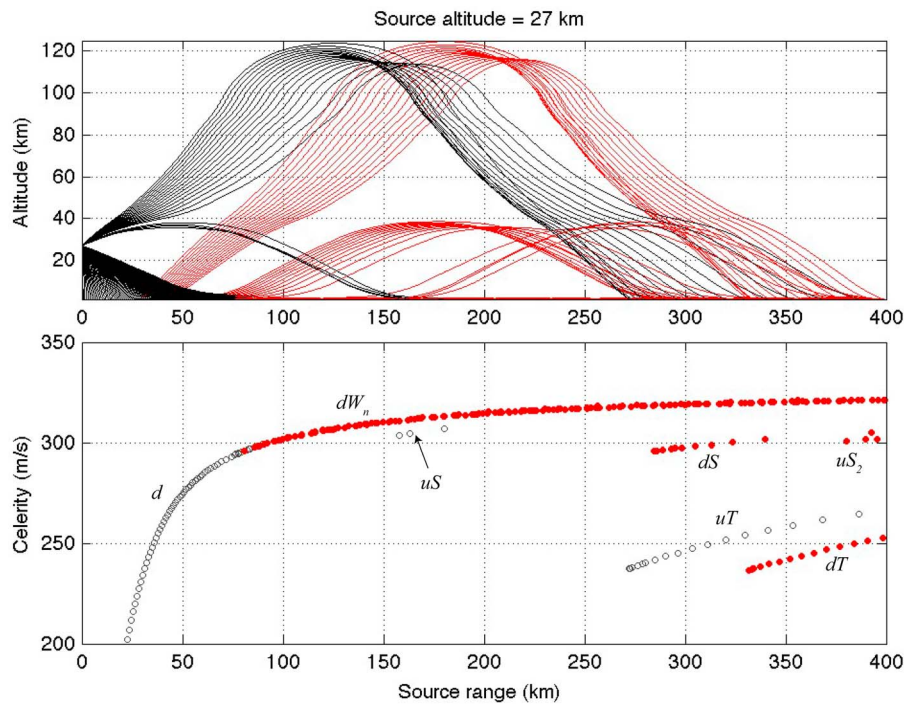


**Figure 8.** (top) Rays shot from the bolide source at an altitude of 27 km along a profile at an azimuth of 210°. Rays that have touched the ground are colored red. (bottom) We plot the celerity of each ray and identify the paths following the nomenclature introduced in Appendix A.

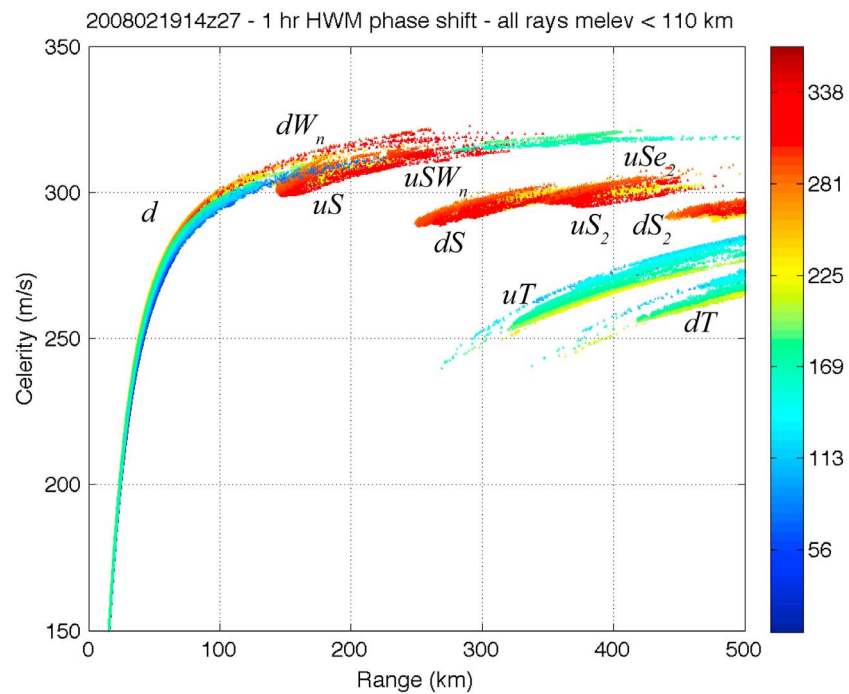


**Figure 9.** Celerity of rays with turning point below 110 km altitude. The rays at ranges under 100 km from the source are direct, down from the source. The predominantly red and yellow rays at ranges above 100 km with celerity near 300 m/s are ducted in the stratosphere. The slower branches seen at ranges above 300 km and celerity above 250 m/s are ducted in the thermosphere. The rays are color-coded by azimuth from the source.

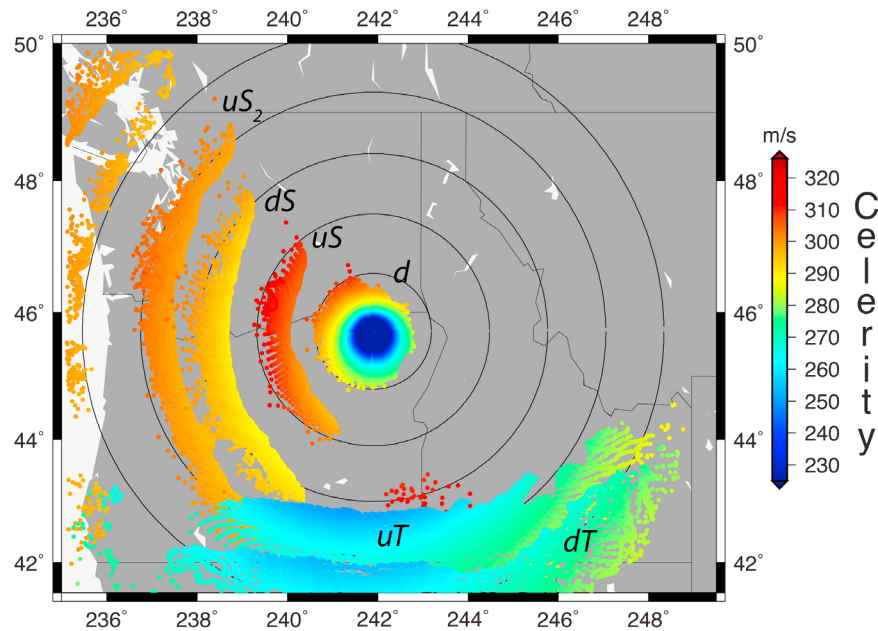


**Figure 10.** Predicted landing points. There are three groups of signals. Close to the source are direct rays down from the source ( $d$ ). To the west, rays with celerity near 290 m/s are stratospherically ducted (including  $uS$ ,  $dS$ ,  $uS_2$ ). The slower signals seen to the south and southeast are ducted in the thermosphere ( $dT$  and  $uT$ ). For clarity, tropospherically ducted energy has not been included in this plot (i.e.,  $dW_n$ ,  $uSW_n$ ,  $uTW_n$ ), where modes interacting with the planetary boundary layer and terrain become trapped near the surface.

(i.e.,  $dS$ ) has a slightly lower celerity of about 300 m/s and is seen starting at ranges of 250 km to the west. More distant clusters of rays, also just predicted to the west of the source, are stratospherically ducted, although the propagation paths are more complicated (i.e.,  $uS_2$ ,  $uSe_2$  and  $dS_2$ ).

[28] The fastest thermospheric branch propagates up from the source ( $uT$ ); the second thermospheric branch lands near the source (as  $d$ ) before ducting back to the ground ( $dT$ ). While classical ray theory predicts that thermospheric ducting should occur in all directions [e.g., *Georges and Beasley, 1977; Drob et al., 2003*], typically only those azimuths where the rays have turning points near or below 110 km should have any appreciable amplitudes (above 0.75 Hz) due to attenuation [e.g., *Sutherland and Bass, 2004*]. Excluding all the rays in the simulation with turning points above 110 km, the thermospheric ducted branches are predicted at celerities below 275 m/s for azimuths to the south. Additional calculations (not shown) indicate that, for these phases, azimuth is a strong function of the phase of solar migrating diurnal and semidiurnal tides [e.g. *Forbes, 1995*]; for example, predominately southeast for 1200 UTC and due west for 1800 UTC. To bring the simulations of the  $uT$  phases into agreement with the observations, the phase of the tides in HWM07 were adjusted forward by 1 h. Furthermore, finite difference modeling confirms that the fourth (slowest) branch was ducted in the thermosphere after being directed up from the source (i.e., no bounce at the free surface between the source and receiving point) (C. D. de Groot-Hedlin, M. A. H. Hedlin, and K. Walker, Numerical synthesis of infrasound propagation with winds and attenuation: Application to a bolide explosion detected by seismic network, submitted to *Geophysical Journal International*, 2010).

[29] The 3-D acoustic ray calculations utilizing the ECMWF/G2S background atmosphere were unable to explain the observation that signals on the third branch predominantly cluster to the south. The investigation of several hypotheses to explain this, related to uncertainties in the atmospheric models in conjunction with limitations of the propagation modeling technique, is ongoing. For example with an artificial adjustment of the southward wind velocity component of about 15 m/s near 60 km with vertical half-width of 10 km over the region, it is possible to produce a secondary branch of arrivals  $uS'$ , very similar to what is observed between ranges of 200 and 300 km with celerities of 260–290 m/s. These are issues are discussed further in section 5.

### 4.3. Spectra

[30] Spectra from acoustic signals have been used to study attenuation and, for example, show significantly higher attenuation in the thermosphere than the stratosphere. We have used acoustic-to-seismic coupled signals in our study, and although the coupling factor is unknown, the receiver response at any given station  $r$  is assumed to be invariant between arrivals. Thus, we assume that each of the multiple acoustic signals recorded at a given station is convolved with the same receiver term. We support this assumption by noting that there is only minor variation in arrival azimuths between signals at a given station and that arrival elevations vary by less than  $20^\circ$  (cf. Figure 8). We adopt a simple model of a signal recording as follows,

$$s_a(t) = b(t) * p_a(t) * r(t),$$

where  $s_a(t)$  is the  $a$ th time domain signal recorded at a site,  $b(t)$  is the bolide source term,  $p_a(t)$  is the infrasound propagation term for the  $a$ th signal,  $r(t)$  is a receiver term, and the asterisk is

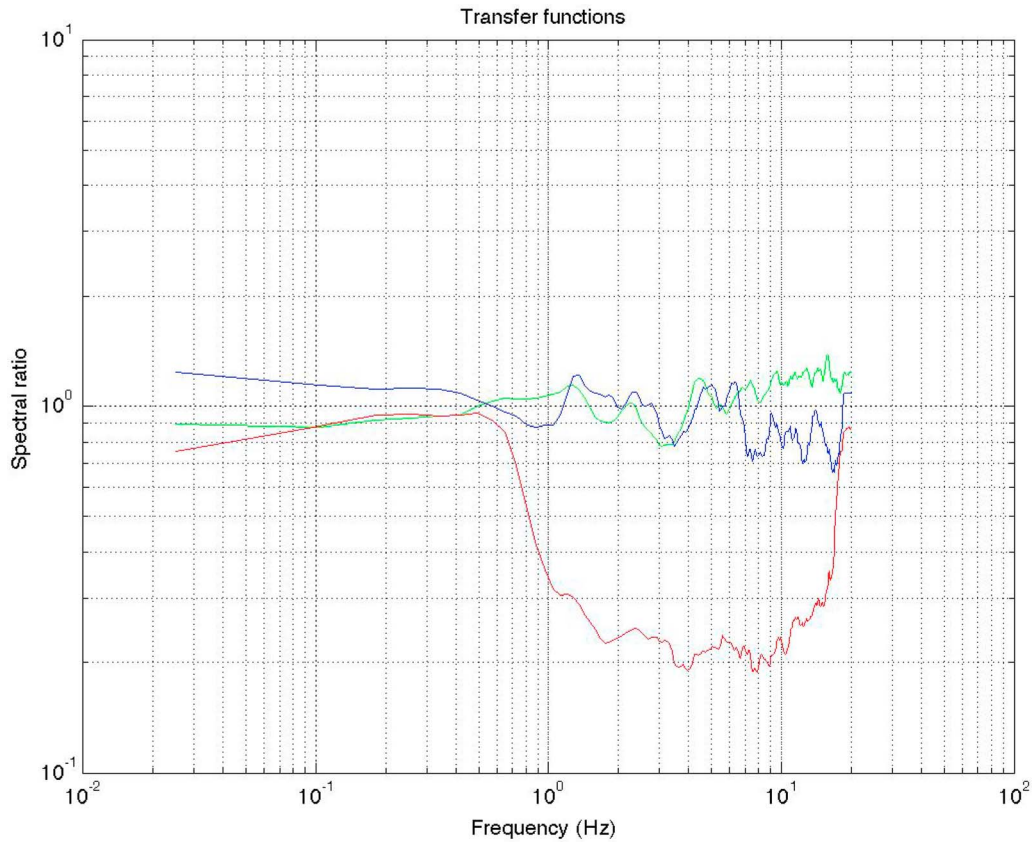


**Figure 11.** Stacked spectral ratios of branches 2, 3, and 4 relative to branch 1 (shown in green, blue, and red, respectively). The stacks were based on data from 79 stations (branch 2 versus branch 1), 29 stations (branch 3 versus branch 1), and 53 stations (branch 4 versus branch 1).

the convolution operator. We assume  $r(t)$  is due to the geology at that site as the instruments are broadband and flat across the frequency band of interest. In the frequency domain this becomes

$$S_a(f) = B(f)P_a(f)R(f),$$

where capitals denote the Fourier transforms. Similarly, for another signal ( $b$ ), we have

$$S_b(f) = B(f)P_b(f)R(f).$$

We concluded earlier that the source of the signals is a terminal explosion and therefore assume here that the source term is omnidirectional. Since the receiver term is invariant with time, a ratio of spectra from two signals recorded by the same seismometer should be equivalent to the ratio of the different propagation terms, i.e.,

$$\frac{S_a(f)}{S_b(f)} = \frac{P_a(f)}{P_b(f)}.$$

We then estimate a transfer function from one path to another,  $T_{ab}(f)$ , by stacking spectral ratios of the two corresponding signals from all stations that recorded both, i.e.,

$$T_{ab}(f) = \frac{1}{N} \sum_1^N \frac{P_a(f)}{P_b(f)}.$$

The assumption is that the paths taken by all signals on a given branch are not significantly different (e.g., all stratospherically

ducted or thermospherically ducted). In our study, we have used smoothed power spectral estimates. We have also used branch 1 as our reference, as the propagation path is relatively simple; at ranges beyond 200 km, the paths are believed to be  $uS$  or  $uSW_n$  (Figure 10).

[31] We show the transfer functions for branch pairs 2/1, 3/1, and 4/1 in green, blue, and red, respectively, in Figure 11. In each case signal, “ $b$ ” is the reference signal from branch 1 (see Figures 5 and 6). If the propagation term for a branch is identical to that of branch 1, the transfer function should be unity at all frequencies. We see that the transfer functions are near unity for pairs 2/1 and 3/1. This suggests that our interpretation of branches 2 and 3 as being stratospherically ducted is correct, since we see no significant difference between these paths and the simpler, presumed stratospheric, first branch. The one outlier is pair 4/1 for frequencies above 0.7 Hz, suggesting more attenuation along path 4, consistent with that expected for a thermospheric branch. As discussed above, ray tracing and finite difference modeling also suggests that branch 4 is thermospheric. We defer a more in depth discussion of propagation and finite difference modeling to de Groot-Hedlin et al. (submitted manuscript).

## 5. Discussion

[32] Ever since warfare has been conducted with large artillery, it has been observed that sound intensity on the ground can be highly variable [Ross, 2000]. Many early

examples of shadow zones are based on verbal accounts of aural observations (for a review, see *de Groot-Hedlin et al.* [2010]). Although instrument recordings confirmed these observations at infrasound frequencies [*Whipple*, 1931; *Gutenberg*, 1939], detailed studies of shadow zones with instruments have been rare. We know that any given propagation path comes with its own shadow zones. Shadow zones from different propagation paths might overlap, or a shadow zone from one path might be infused by sound that propagated along a different path. As the spatial limits of shadow zones vary, the area in which the sound that propagated along a particular path reaches the ground will also vary, and therefore some sources may be detected more than once.

[33] Today, we collect high-quality data at sample rates well above 1 Hz, allowing us to study wavetrains across a broadband extending to the high-infrasound range. Processing array recordings gives much *local* control on other signal characteristics (most notably velocity). Although we have more infrasound arrays in operation than at any time in history, the recording network is still relatively sparse. Our sampling of the infrasound wavefield from any source is irregular, and each array can only be regarded as providing a spot measurement. We can only infer the spatial structure of the infrasound wavefield from such a sparse network, much like how a geologist can infer the structure of a sedimentary basin by analyzing samples of rock from a few drill holes. Infrasound arrays give us a tantalizing, but very incomplete, sampling of the infrasound wavefield. Much like in oil exploration where dense lines of geophones are used to record active sources and fill in the blanks between points of ground truth (drill holes), it seems important that we infill the large gaps between infrasound arrays in an effort to probe much more deeply the nature of sound propagation.

[34] One could easily point out that seismic instruments are not ideal tools for atmospheric research. Seismometers do not directly record atmospheric pressure variations but record, faithfully, how the Earth moves. For our type of study, seismometers record how the ground responds to loading of the Earth's surface by atmospheric pressure variations due to a source above the ground. We assume that the local site response is imprinted on the pure acoustic signal as coupling from acoustic to seismic occurs. Stations in the USArray provided most recordings used in this study. A key design feature of the USArray is that bedrock sites have been avoided; all stations are deployed above sediments. The goal was to deploy a network that would respond to incident seismic signals as uniformly as possible. Although for this reason we do not expect a significant variation in acoustic-to-seismic coupling between adjacent stations or across the entire network of stations, the results of our analyses do not require an assumption regarding the material properties beneath each station. Furthermore, we do not know if the energy clearly recorded in the seismic networks is due to the acoustic-to-seismic conversion phenomenon or if it is related to a mechanical sensor effect due to the passing pressure wave. Our analyses do not require either of these assumptions, because we simply picked the onset time of energy on the seismograms that move out between a minimum and maximum moveout velocity (intentionally without guidance from ray tracing) and have identified stations for which there was no energy observed. We show spatial patterns in these observations and nonobservations that match fairly well to

those predicted by 3-D ray tracing using an ECMWF model. Quite simply, this favorable comparison between predictions and observations (Figure 7) indicates that there are no significant site-to-site variations in geology that affect our results.

[35] Because the sound speed is relatively slow, we now evaluate the effect of source location inaccuracies on our results. The main metric used to determine "goodness of fit" between our predictions and observations is celerity. Most stations have a range greater than 100 km. At such ranges, travel time is more sensitive to source latitude and longitude than source altitude. As detailed in a companion paper by *Walker et al.* [2010], the uncertainty in X/Y source location is quantified, via reverse time migration with a bootstrap method, by a 95% uncertainty ellipse that is 13 km long by 2 km wide. The optimum location is close to the center of this ellipse and is 2 km from the source location provided by video camera back azimuth observations. Using just first arrival picks within 87 km of this source location, we solve for altitude and source time using 3-D ray tracing in another grid search. The source time is resolved perfectly (matches the video time stamp of the flash to within 0.5 s). The source altitude has an uncertainty of  $\pm 3$  km. Source mislocation errors in latitude and longitude will map into observed celerity errors in Figure 7. However, these inaccuracies will decrease with increasing range. For example, if we assumed a source location that was actually 5 km farther to the east, we would expect, at a range of 100 km, a celerity inaccuracy that varies as a function of azimuth from +14 m/s in the east to 0 m/s in the north and south directions to -14 m/s in the west. In Figure 7a, we do observe changes in celerity within the first 100 km (mostly due to hyperbolic moveout associated with a stratospheric source altitude); however, the range is quite variable for these stations, making such an evaluation of source inaccuracy difficult. However, for a range of 300 km, the azimuthally dependent celerity inaccuracy from north to west would span 5 m/s. This 5 m/s variation is within the scatter of the observed celerities, suggesting that the source is relatively well located and that our results are reliable.

[36] Taking care to avoid aspects of the seismic data that are uncertain, we have found that the signal onsets recorded at a nearly continuous function of range and azimuth from the bolide source help to fill in the blanks between the infrasound arrays. In this study, the blanks are huge; within 500 km of the source, there was just a single infrasound array. With the blanks filled in, we have been able to observe with detail and high confidence several branches of infrasound propagation from the bolide source to a range of 500 km. As discussed by *Walker et al.* [2010], stacking techniques clearly reveal branches to 800 km from this event.

[37] Bolides propagate well above Mach 1 (4–70 km/s) [*ReVelle*, 1997; *Taylor and Elford*, 1998]. Before we interpret the branches, can we be confident that we are observing a point source (the terminal burst) and not sound shed from the line source that came before? This is always a valid question in infrasound studies of bolides [e.g., *ReVelle*, 1997; *Edwards*, 2010]. As is shown in *Walker et al.* [2010], video data point to a flash location that is within 2 km of the seismic location (Figure 2). Furthermore, if the signals used to locate the source originated from the Mach cone, the source location uncertainties would not be as small. Although

we have not attempted to accurately constrain the entry path of the bolide as was done by *Langston* [2004], a cursory inspection of the video data indicates the bolide approached its burst point from the north. Cameras in Portland (to the west of the terminal burst) and Boise (to the southeast) provided the strongest evidence for this claim [*Walker et al.* 2010]. We have not observed any arrivals that have moveout velocities consistent with a supersonic line source. We expect that a signal from the Mach cone exists but is much smaller and embedded in the larger signals from the terminal burst.

[38] We have presented our analysis of a large database of signal arrival times from a point source. We have observed the spatial extent of infrasound branches from the source. We have observed variations of the celerity of the branches with range, the relative timing of the branches at a nearly continuous function of range, and the amplitude of the branches as a function of range and azimuth with respect to background noise (Figure 6). Observing acoustic branches evolve across great distances spanned by relatively dense seismic networks rather than “spot” checking them at isolated points provides a deeper understanding of the nature of long-range infrasound propagation and permits more rigorous tests of our atmospheric models, models that are essential for infrasound research. These atmospheric infrasound branches are somewhat reminiscent of branches of seismic signals (such as mantle phases and core phases) that are readily studied with seismic networks [e.g., *Shearer*, 1991].

[39] From the standpoint of acoustic propagation physics, this event is particularly interesting because it occurred during a sudden stratospheric warming when that atmosphere was in a dynamically unstable state. The observed branches extend almost exclusively to the west, southwest, and northwest of the source and not to the east, as normally expected at this location during the winter. Other such events have also been recently observed by *Evers and Siegmund* [2009] and predicted by *Drob et al.* [2010b].

[40] As suggested by *Le Pichon et al.* [2005], *Drob et al.* [2010b], and the results presented here, the comparison of observed and predicted infrasound arrivals provides a means to corroborate related observations, resolving discrepancies between the various high-latitude specifications. Typical uncertainties of the available atmospheric specifications models are on the order of 5–7 m/s in this altitude region, increasing to perhaps even 10 m/s under certain conditions, with these uncertainties pertaining to the average wind fields over some finite time interval and model grid cell. Available atmospheric specifications do not attempt to deterministically resolve subgrid scale structures, such as localized atmospheric gravity waves that may increase these uncertainties slightly. In addition, the wind fields in these models at these altitudes are not derived from direct routine global wind measurements but instead are the result of the assimilation of global satellite-based temperature soundings in the global equations of fluid dynamics. On average, the values in the available models are accurate (as described in the aforementioned references), but locally under the rapidly changing dynamical conditions of a sudden stratospheric warming where planetary wave-scale wave-breaking events occur, it is not unreasonable to think that specifications have greater uncertainty/less accuracy in the affected regions. As described by *Manney et al.* [2008], in the limited geographic

region affected by the sudden stratospheric warming’s (SSW), current high-latitude data assimilation systems (e.g., ECMWF, GEOS5) [*Rienecker et al.*, 2008] produce accurate specifications below 60 km, but existing systems have occasional difficulties above 60 km. However, even during SSW conditions, winds provided by existing data assimilation systems should be more accurate than any climatological specification, which is simply based on averages of historical data (CIRA86 [*Fleming et al.*, 1988] and HWM07 [*Drob et al.*, 2008]). In general, the ECMWF model for this event provides the predictions that agree the most with our observed arrivals, despite its inability to predict one of the branches.

[41] In addition, the variations of the backazimuth of the contact points of the thermospherically ducted signals are governed by the phase of the diurnal and semidiurnal migrating tides. The upward-propagating diurnal and semidiurnal tides are a vertically polarized gravity wave with vertical wavelengths on the order of 20 km [e.g., *Forbes*, 1995]. As result, the direction of maximum winds at a given altitude (e.g., 110 km) rotates in azimuth with the phase of the migrating tides. Consequently, the azimuth, for which thermospherically ducted waves will have the lowest turning point and thus undergo the least attenuation, will also rotate in azimuth around a given source location with local time. This effect was first observed by *Donn and Rind* [1972] and recently revisited by *Le Pichon et al.* [2005], where the detection of thermospheric modes along a fixed back azimuth depends on local time, even though the source characteristics remained independent of local time. Furthermore, for certain geographic locations and times/seasons, the dynamical variability of the upper mesospheric and thermospheric modes may be even greater than can be presently calculated by the combination of the ECMWF and HWM07 models; particularly after accounting for observed and documented nonmigrating tides [*Forbes et al.*, 2003], day-to-day and interseasonal tidal variability [*Fritts and Isler*, 1994; *Lieberman et al.*, 2007], and the existence of vertically propagating and stationary mesosphere lower thermosphere planetary waves [*Smith*, 1996; *McLandress et al.*, 2006].

[42] With respect to the inability to completely explain the third branch of arrivals in Figure 6, the problem may not simply be related to errors in the atmospheric specifications as provided. Other issues involve assumptions made about the propagation physics, including not properly accounting for the presence of the subgrid scale internal gravity wavefield [*Chunchuzov*, 2004; *Kulichkov et al.*, 2008], as well as nonlinear acoustic wave propagation effects [*Millet et al.*, 2007]. The results in Figure 10 show several discrete bands of detections with classically predicted shadow zones, while the observations shown in Figure 3 indicate a continuous distribution of detections at all ranges. This is most likely the result of ignoring the subgrid scale internal gravity wave spectrum fluctuations in our forward calculations, but such calculations are beyond the current discussion and are planned for a follow on publication. Preliminary modeling with a 2-D model seems to support this conclusion. Furthermore, the calculations suggest that modification of the propagation physics by accounting for gravity wave fluctuations may also explain those differences between the predicted and observed arrival branches, such as the third observed branch in Figure 6.

[43] Atmospheric shadow zones have been known to exist for a long time. In the high-frequency ray approximation, rays refract away from regions of higher wave speed. Upward refraction can be due to either an increase in temperature or wind speed with altitude. The former results in an isotropic shadow zone with a width that is purely a function of source height and range; a wind-induced shadow zone is anisotropic, with a fairly quick decay of signal energy as a function of source–receiver azimuth at some roughly constant range. Within the resolution of the uneven station distribution, this predicted decay is what is observed in branches 1 ( $uS$ ) and 2 ( $dS$ ) in Figures 5c, 7a, and 7b and predicted in Figure 10. At a range of about 300 km, the first and second branches are observed to decrease in energy from an azimuth of  $195^\circ$ – $180^\circ$  (representing a distance of 50–100 km). The northern extent of branch 2 is also consistent with that predicted, although the northern edge of branch 1 is poorly defined. These consistencies suggest that the high-frequency ray approximation works well and that both diffraction and scattering played a minor role, if any, at these frequencies in this wind-induced shadow zone.

[44] Although the location of the azimuthal decay of energy is well predicted by the ray tracing, the location of the expected decay of energy with range is not fully consistent with that predicted. For example, the innermost edge of branch 2 in Figure 7b is along the 200 km radius. This edge is predicted to be 50 km further to the west (Figure 10). Although this significant deviation may be simply explained by inaccuracies in the velocity model, the observed effect of diffraction or turbulent scattering could also be an anisotropic phenomenon, imparting a greater influence in the spatial decay rate downwind of the source than in a crosswind direction.

## 6. Conclusions

[45] The 2008 Oregon bolide was registered by hundreds of seismometers to a range of several hundreds of kilometers illuminating detection patterns in range and azimuth at a level of detail unattainable by conventional global infrasound arrays. A sudden stratospheric warming event reversed the winds and caused unexpected ducting to the west. Three-dimensional ray tracing with a range-dependent G2S model resolves the majority of these observations. Other perturbations to the velocity model due to tidal factors and gravity waves may explain the minor discrepancies between the observed and predicted branches.

[46] Although one must use caution when interpreting amplitudes, the remarkable consistency in the observed and predicted first arrival time patterns suggest that they accurately illuminate shadow zones due to the influence of the westward winds associated with the sudden stratospheric warming. The azimuthal edges of these shadow zones appear to be better predicted than the range edges for the stratospherically ducted phases. However, there is arguably better azimuth resolution than range resolution due to an uneven station distribution.

[47] The ray tracing predicted a wide distribution for thermospheric arrivals. The observed arrivals that had thermospheric characteristics encompassed a much smaller area. We interpret this observation to be due to wind speed fluctuations in the lower thermosphere that were not captured in the G2S

model, specifically the amplitude and phase of diurnal tidal components encapsulated in HWM07. These fluctuations gave rise to earlier than predicted returns that took significantly different raypaths than those predicted to have returned from turning points at higher altitudes in the thermosphere, which would have been more attenuated and perhaps below the seismic network noise floor.

[48] Although seismic networks have traditionally been designed just to probe downward to examine the Earth's interior structure and to study seismic sources, it seems clear that such data can provide valuable information about atmospheric sources and the structure of the atmosphere. The information can be useful, provided the signals are abrupt and recorded well above noise; however, it would always be preferable to directly record acoustic signals free of concern about acoustic-to-seismic coupling. In addition, any geophysical source near the Earth's free surface can potentially emit both upgoing acoustic energy and downgoing seismic energy. It seems clear that our understanding of the physics of such a 3-D source would remain incomplete if we rely on just one type of sensor, either acoustic or seismic. The two fields, seismology and atmospheric acoustics, are clearly interconnected. Perhaps as more examples of this interconnectedness come available there will be increased interest in colocating seismic and acoustic sensors and collecting true broadband atmospheric pressure data at a density that will permit real progress in our understanding of infrasound propagation.

## Appendix A: New Nomenclature for Infrasound Propagation

[49] We have extended the nomenclature of *Brown et al.* [2002] to allow us to represent any arbitrary path through the atmosphere from an infrasound source to a receiver on the ground with a simple-coded term. A coded term that is assigned to such a path is constructed by the following simple rules. We define a basic term to represent a simple propagation path. Any complex path is broken down into a sequence of simple segments between the source and receiver, and the term that represents the entire path is simply a concatenation of basic terms that represent each simple segment of the overall path. The order in which the overall code is constructed from left to right reflects the order of propagation segments beginning with the source and ending at the receiver. The approach is not new. The global seismology community has used such a nomenclature to describe seismic propagation through the solid Earth for decades. We feel it is time that we have a corresponding nomenclature to describe propagation paths in the atmosphere above the solid Earth.

[50] We begin with the basic nomenclature of *Brown et al.* [2002], i.e., we use the letter  $W$  to represent infrasound ducted in the troposphere. Similarly, we use the letters  $S$  and  $T$  to represent sound ducted in the stratosphere and in the thermosphere, respectively. This is a slight departure from *Brown et al.* [2002] in that the terms do not include the letter  $I$  to signify infrasound propagation. It is implicit that our terms represent infrasound paths. It is also implicit when the terms  $W$ ,  $S$ , and  $T$  are used that the lower bound of the duct is the Earth's free surface. Special terms are introduced later that describe propagation in an elevated duct.

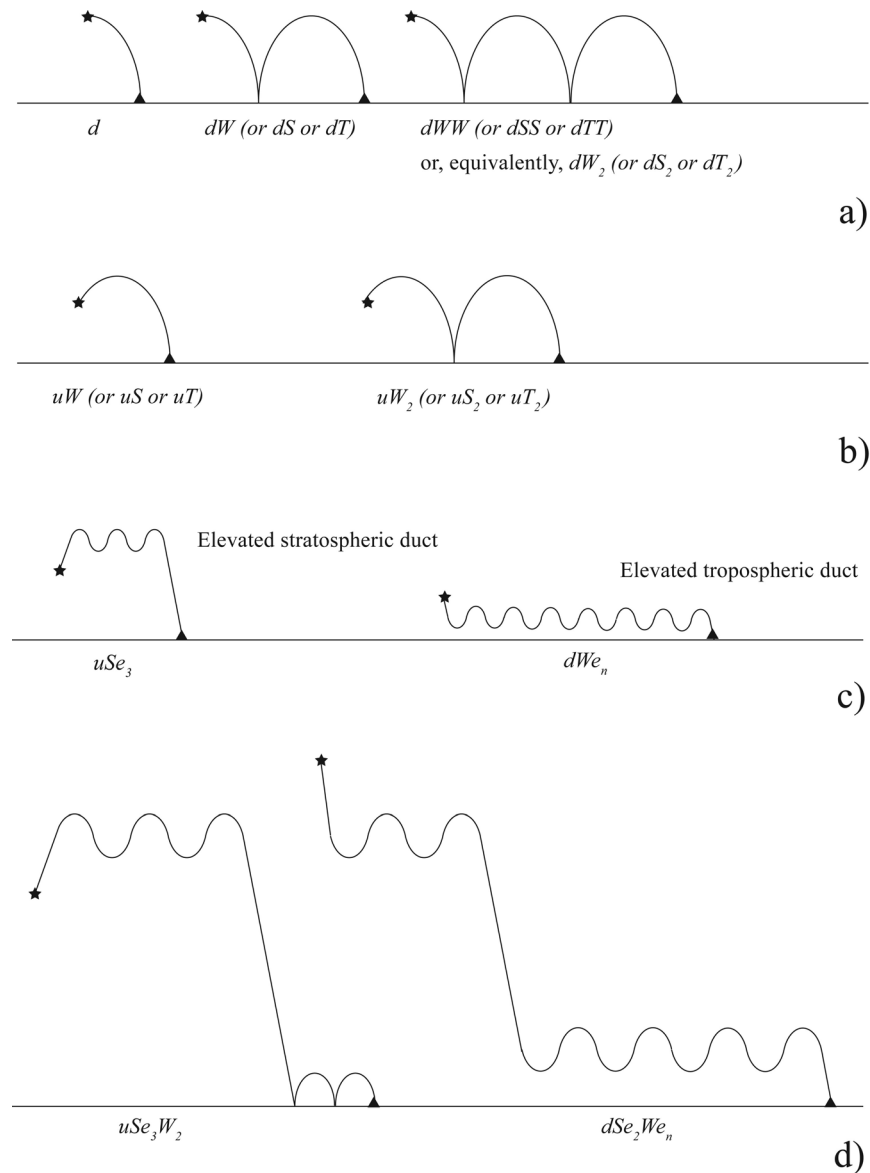


**Figure A1.** Diagrams illustrating terms assigned to various infrasound propagation paths. (a) Simple paths down from an elevated source. (b) Simple paths up from a source. Neither of these figures has a vertical scale. The ducts depicted could be tropospheric, stratospheric, or thermospheric. (c) Simple propagation paths through elevated ducts. (d) The terms representing more complex propagation paths are constructed by concatenating subterms representing simple path segments.

[51] A prefix to each coded term describes the direction of sound propagation as it leaves the source. The letter  $u$  represents sound propagating up from the source, and the letter  $d$  represents sound propagating down.

[52] As shown in Figure A1, we therefore represent simple propagation down from the source to the ground with the letter  $d$ , regardless of the altitude of the source. This is the one special path in our nomenclature which is entirely described just by its direction leaving the source. The term  $dW$  represents propagation down from the source followed by one leg of the overall path ducted in the troposphere. The term  $dWW$  represents a path like  $dW$ , except there is one additional reflection at the Earth's surface and one extra turn in the troposphere. A more compact form we prefer to

describe paths that involve multiple turns in one duct uses a subscript to represent the number of turns. Therefore,  $dWW$  is written more compactly as  $dW_2$ , a notation that is certainly preferred for paths that involve many turns in a layer. With this in mind, to describe an arbitrarily large, and perhaps unknown, number of turns in the duct, we use the term  $dW_n$ . Using this basic structure, we describe propagation through a stratospheric duct or a thermospheric duct by replacing the letter " $W$ " with a  $S$  or with a  $T$ , respectively (as shown in Figure A1a).

[53] For a path in which the energy is directed upward from the source and turns once before reaching the ground, we would use  $uW$  to represent energy ducted once in the troposphere and  $uS$  and  $uT$  represent upward energy ducted

in the stratosphere and the thermosphere, respectively (refer to Figure A1b).

[54] Energy trapped in an elevated duct is described with the same basic structure; however, we use the terms  $We$ ,  $Se$ , and  $Te$  to represent elevated tropospheric, stratospheric, and thermospheric ducts, respectively. Figure A1c shows two simple examples of terms assigned to paths involving elevated ducts.

[55] With these basic components, we can now describe arbitrarily complex infrasound propagation paths. A path (shown in Figure A1d) up from a source that turns 3 times in an elevated stratospheric duct before exiting the duct and then becoming ducted twice in a ground level tropospheric duct is represented by the term  $uSe_3W_2$ . A path down from a source above the stratosphere ducted twice in an elevated stratospheric duct, then leaking out into an elevated tropospheric duct in which the number of turns is large and unknown is described as  $dSe_2We_n$  (as shown in Figure A1d).

[56] Finally, referring to Brown *et al.* [2002], we represent the Lamb surface wave simply with the term  $L$ .

[57] **Acknowledgments.** This study would not have been possible without generous contributions from a large group of people. We are deeply indebted to Matt Fouch (University of Arizona) and David James (Carnegie Institution of Washington) for giving us access to data from their High Lava Plains Seismic Experiment. We are also very much indebted to Gene Humphries (University of Oregon) for giving us access to data from the Wallowa Flexible Array Experiment. We would like to extend our deep appreciation to Jeffrey Brower of the Global Meteor Scatter Network for providing us with the video from his all-sky camera in West Kelowna, British Columbia, and his estimate of the azimuth to the terminal burst. We would like to thank Alan Hildebrand of the University of Calgary and Don Hladiuk for providing us with the Calgary all-sky video and terminal burst time. In particular, we would like to acknowledge Earthscope and IRIS for the data from USArray, without which this study would not have been possible. The ECMWF data have been kindly provided by the Provisional Technical Secretariat of CTBTO solely for the purpose of CTBT-related scientific and technical activities. We frequently used Boulder Real-Time Technologies Antelope software to analyze the data. We would like to extend our deep appreciation to two anonymous reviewers who provided insightful comments and made numerous suggestions that strengthened our paper. This publication was made possible through the support provided by the U.S. Army Space and Missile Defense Command. The opinions expressed herein are those of the authors and do not necessarily reflect the views of the U.S. Army Space and Missile Defense Command.

## References

- Arrowsmith, S. J., R. Whitaker, R. Burlacu, B. Stump, M. A. H. Hedlin, G. Randall, C. Hayward, and D. ReVelle (2008), Regional monitoring of infrasound events using multiple arrays: Application to Utah and Washington State, *Geophys. J. Int.*, **175**, 291–300.
- Bass, H., J. Bhattacharyya, M. Garces, M. A. H. Hedlin, J. Olson, and R. Woodward (2006), Infrasound, *Acoust. Today*, **2**, 9–19.
- Bedard, A., and T. M. Georges (2000), Atmospheric infrasound, *Phys. Today*, **53**, 32–27.
- Brown, D., C. N. Katz, R. Le Bras, M. P. Flanagan, J. Wang, and A. K. Gault (2002), Infrasonic signal detection and source location at the prototype international data centre, *Pure Appl. Geophys.*, **159**, 1081–1125.
- Chunchuzov, I. P. (2004), Influence of internal gravity waves on sound propagation in the lower atmosphere, *Meteorol. Atmos. Phys.*, **85**, 61–76.
- Cochran, E. S., and P. M. Shearer (2006), Infrasound events detected with the southern California seismic network, *Geophys. Res. Lett.*, **33**, L19803, doi:10.1029/2006GL026951.
- de Groot-Hedlin, C. D. (2008), Finite-difference synthesis of infrasound propagation through an absorbing atmosphere, *J. Acoust. Soc. Am.*, **124**, 1430–1441.
- de Groot-Hedlin, C. D., M. A. H. Hedlin, K. Walker, D. Drob, and M. Zumberge (2008), Study of propagation from the shuttle Atlantis using a large seismic network, *J. Acoust. Soc. Am.*, **124**(3), 1442–1451.
- de Groot-Hedlin, C. D., M. A. H. Hedlin, and D. Drob (2010), Atmospheric variability and infrasound monitoring, in *Infrasound Monitoring for Atmospheric Studies*, edited by A. Le Pichon, E. Blanc, and A. Hauchecorne, pp. 475–510, Springer, Dordrecht.
- Donn, W. L., and D. Rind (1972), Microbaroms and the temperature and winds in the upper atmosphere, *J. Atmos. Sci.*, **29**, 156–172.
- Drob, D. P., J. M. Picone, and M. Garcés (2003), Global morphology of infrasound propagation, *J. Geophys. Res.*, **108**(D21), 4680, doi:10.1029/2002JD003307.
- Drob, D. P., et al. (2008), An empirical model of the Earth's horizontal wind fields: HWM07, *J. Geophys. Res.*, **113**, A12304, doi:10.1029/2008JA013668.
- Drob, D. P., R. R. Meier, J. M. Picone, and M. Garces (2010a), Inversion of infrasound signals for passive atmospheric remote sensing, in *Infrasound Monitoring for Atmospheric Studies*, edited by A. Le Pichon, E. Blanc, and A. Hauchecorne, pp. 701–732, Springer, Dordrecht.
- Drob, D. P., M. Garcés, M. A. H. Hedlin, and N. Brachet (2010b), The temporal morphology of infrasound propagation, *Pure Appl. Geophys.*, doi:10.1007/s00024-010-0080-6.
- Edwards, W. (2003), SUPRACENTER: Determining locations of fireball terminal bursts using seismic arrival times of acoustic waves, Ph.D. thesis, Univ. of Calgary, Calgary, Alberta, Canada.
- Edwards, W. (2010), Meteor generated infrasound: Theory and observation, in *Infrasound Monitoring for Atmospheric Studies*, edited by A. Le Pichon, E. Blanc, and A. Hauchecorne, pp. 361–414, Springer, Dordrecht.
- Evers, L. G., and P. Siegmund (2009), Infrasonic signature of the 2009 major sudden stratospheric warming, *Geophys. Res. Lett.*, **36**, L23808, doi:10.1029/2009GL041323.
- Fleming, E. L., S. Chandra, M. R. Shoerberl, and J. J. Barnett (1988) Monthly Mean Global Climatology of Temperature, Wind, Geopotential Height and Pressure for 0–120 km, Natl. Aero. and Space Admin., Tech. Memo. 100697, Washington, D. C.
- Forbes, J. M. (1995), Tidal and Planetary Waves, in *Geophysical Monograph on the Upper Mesosphere and Lower Thermosphere*, edited by R. M. Johnson, and T. L. Killeen, AGU, Washington, D. C.
- Forbes, J. M., X. L. Zhang, E. R. Talaat, and W. Ward (2003), Nonmigrating diurnal tides in the thermosphere, *J. Geophys. Res.*, **108**(A1), 1033, doi:10.1029/2002JA009262.
- Fritts, D. C., and J. R. Isler (1994), Mean motions and tidal and 2 day structure and variability in the mesosphere and lower thermosphere over Hawaii, *J. Atmos. Sci.*, **51**, 2145–2164.
- Garcés, M., M. Willis, C. Hetzer, and D. Drob (2004), On using ocean swells for continuous infrasonic measurements of winds in the lower, middle, and upper atmosphere, *Geophys. Res. Lett.*, **31**, L19304, doi:10.1029/2004GL020696.
- Georges, T. M., and W. H. Beasley (1977), Refraction of infrasound by upper-atmospheric winds, *J. Acoust. Soc. Am.*, **61**, 28–33, doi:10.1121/1.381263.
- Georges, T. M., and J. M. Young (1972), Passive sensing of natural acoustic-gravity waves at the Earth's surface, in *Remote Sensing of the Troposphere*, edited by V. E. Derr, chap. 21, U. S. Gov. Print. Office, Washington, D. C.
- Gibson, R., D. Drob, and D. Broutman (2009), Advancement of techniques for modeling the effects of fine-scale atmospheric inhomogeneities on infrasound propagation, in *Proceedings of the 2009 Monitoring Research Review: Ground-Based Nuclear Explosion Monitoring Technologies, LA-UR-08-05276*, U. S. Govt., pp. 714–728.
- Gossard, E. E., and W. H. Hooke (1976), *Waves in the Atmosphere*, 456 pp., Elsevier, Amsterdam, Netherlands.
- Green, D., and D. Bowers (2009), Estimating the detection capability of the international monitoring system infrasound network, paper presented at 2009 International Scientific Studies Conference, p. 50, Vienna, Austria, 10–12 June.
- Gutenberg, B. (1939), The velocity of sound waves and the temperature in the stratosphere in Southern California, *Bull. Seismol. Soc. Am.*, **20**, 192–201.
- Hastings, D. A., et al. (1999), The Global Land One-kilometer Base Elevation (GLOBE) Digital Elevation Model, ver. 1.0., Natl. Oceanic and Atmos. Admin., Natl. Geophys. Data Center, Boulder, Colo. (Available at <http://www.ngdc.noaa.gov/mgg/topo/globe.html>)
- Hedlin, M. A. H. (2006), *Infrasound, Yearbook of Science and Technology*, pp. 163–166, McGraw-Hill.
- Herrin, G., et al. (2008), High-altitude infrasound calibration experiments, *Acoust. Today*, **4**, 9–21.
- Kanamori, H., J. Mori, D. L. Anderson, and T. H. Heaton (1991), “Seismic excitation by the space shuttle Columbia,” *Nature*, **349**, 781–782, doi:10.1038/349781a0.
- Kulichkov, S. N., I. P. Chunchuzov, G. A. Bush, and V. G. Perepelkin (2008), Physical modeling of long-range infrasonic propagation in the atmosphere, *Izvestiya Atmos. Oceanic Phys.*, **44**, 175–186.
- Langston, C. (2004), Seismic ground motions from a bolide shock wave, *J. Geophys. Res.*, **109**, B12309, doi:10.1029/2004JB003167.

- Le Pichon, A., M. Garces, E. Blanc, M. Barthelemy, and D. Drob (2002a), Acoustic propagation and atmosphere characteristics derived from infrasonic waves generated by the Concorde, *J. Acoust. Soc. Am.*, *111*, 629–641.
- Le Pichon, A., J. Guilbert, A. Vega, M. Garces, and N. Brachet (2002b), Ground-coupled air waves and diffracted infrasound from the Arequipa earthquake of June 23, 2001, *Geophys. Res. Lett.*, *29*(18), 1886, doi:10.1029/2002GL015052.
- Le Pichon, A., E. Blanc, D. Drob, S. Lambotte, J.X. Dessa, M. Lardy, P. Bani, and S. Vergnolle (2005), Infrasound monitoring of volcanoes to probe high-altitude winds, *J. Geophys. Res.*, *110*, D13106, doi:10.1029/2004JD005587.
- Le Pichon, A., J. Vergoz, E. Blanc, J. Guilbert, L. Ceranna, L. Evers, and N. Brachet (2009), Assessing the performance of the International Monitoring System's infrasound network: Geographic coverage and temporal variabilities, *J. Geophys. Res.*, *114*, D08112, doi:10.1029/2008JD010907.
- Lieberman, R. S., D. M. Riggan, D. A. Ortland, S. W. Nesbitt, and R. A. Vincent (2007), Variability of mesospheric diurnal tides and tropospheric diurnal heating during 1997–1998, *J. Geophys. Res.*, *112*, D20110, doi:10.1029/2007JD008578.
- Long, M., H. Gao, A. Klaus, L. Wagner, M. Fouch, D. James, and E. Humphreys (2009), Shear wave splitting and the pattern of mantle flow beneath eastern Oregon, *Earth Planet. Sci. Lett.*, doi:10.1016/j.epsl.2009.09.039.
- Manney, G. L., et al. (2008), The evolution of the stratopause during the 2006 major warming: Satellite data and assimilated meteorological analyses, *J. Geophys. Res.*, *113*, D11115, doi:10.1029/2007JD009097.
- McLandsess, C., W. E. Ward, V. I. Fomichev, K. Semenuik, S. R. Beagley, N. A. McFarlane, and T. G. Shepherd (2006), Large-scale dynamics of the mesosphere and lower thermosphere: An analysis using the extended Canadian Middle Atmosphere Model, *J. Geophys. Res.*, *111*, D17111, doi:10.1029/2005JD006776.
- Mikumo, T. (1968), Atmospheric pressure waves and tectonic deformation associated with the Alaskan earthquake of March 28, 1964, *J. Geophys. Res.*, *73*(6), 2009–2025, doi:10.1029/JB073i006p02009.
- Millet, C., J.-C. Robinet, and C. Roblin (2007), On using computational aeroacoustics for long-range propagation of infrasounds in realistic atmospheres, *Geophys. Res. Lett.*, *34*, L14814, doi:10.1029/2007GL029449.
- Norris, D., R. Gibson, and K. Bongiovanni (2010), Numerical methods to model infrasonic propagation through realistic specifications of the atmosphere, in *Infrasound Monitoring for Atmospheric Studies*, edited by A. Le Pichon, E. Blanc, and A. Hauchecorne, pp. 541–574, Springer, Dordrecht.
- Persson, A., and F. Grazzini (2007), User Guide to ECMWF forecast products, *ECMWF Meteorological Bulletin M3.2*. (Available at <http://www.ecmwf.int/products/forecasts/guide>)
- Picone, J. M., A. E. Hedlin, D. P. Drob, and A. C. Aikin (2002), NRLMSISE-00 empirical model of the atmosphere: Statistical comparisons and scientific issues, *J. Geophys. Res.*, *107*(A12), 1468, doi:10.1029/2002JA009430.
- Rienecker, M. M., et al. (2008), The GEOS-5 Data Assimilation System—Documentation of versions 5.0.1, 5.1.0, and 5.2.0, *NASA/Tech. Memo. 2008-104606*, 27, 93.
- ReVelle, D. O. (1997), Historical detection of atmospheric impacts of large superbolides using acoustic-gravity waves, *Ann. N. Y. Acad. Sci.*, *822*, 284–302.
- Rogers, R. M., A. Sauter, R. W. Busby, T. Kim, C. Hayward, and B. W. Stump (2008), Infrasound observations at USArray sites—A preliminary investigation of the utility of seismo-acoustic observations on a regional scale, *Eos Trans. AGU*, *89*(53), Fall Meet. Suppl., Abstract S33B-1944.
- Ross, C. D. (2000), Outdoor sound propagation in the US Civil War, *Appl. Acoust.*, *59*, 137–147.
- Scarberry, K., A. Meigs, and A. Grunder (2009), Faulting in a propagating continental rift: Insight from the late Miocene structural development of the Abert Rim fault, southern Oregon, USA, *Tectonophysics*, doi:10.1016/j.tecto.2009.09.025.
- Shearer, P. M. (1991), Imaging global body wave phases by stacking long-period seismograms, *J. Geophys. Res.*, *96*(B12), 20,353–20,364, doi:10.1029/91JB00421.
- Smith, A. K. (1996), Longitudinal variations in mesospheric winds: Evidence for gravity wave filtering by planetary waves, *J. Atmos. Sci.*, *53*, 1156–1173.
- Sutherland, L. C., and H. E. Bass (2004), Atmospheric absorption in the atmosphere up to 160 km, *J. Acoust. Soc. Am.*, *115*, 1012–1032.
- Symons, G. J. (Ed.) (1888), *The eruption of Krakatoa and subsequent phenomena, Report of the Krakatoa committee of the Royal Society*, 494 pp., Harrison and Sons, St. Martin's Lane, W.C.
- Taylor, A. D., and W. G. Elford (1998), Meteoroid orbital element distributions at 1 AU deduced from the Harvard Radio Meteor Project observations, *Earth Planets Space*, *50*, 569–575.
- Walker, K., M. A. H. Hedlin, C. D. de Groot-Hedlin, J. Vergoz, A. Le Pichon, and D. Drob (2010), Source location of the 19 February 2008 Oregon bolide using seismic networks and infrasound arrays, *J. Geophys. Res.*, doi:10.1029/2010JB007863, in press.
- Wang, L., and M. J. Alexander (2009), Gravity wave activity during stratospheric sudden warmings in the 2007–2008 Northern Hemisphere winter, *J. Geophys. Res.*, *114*, D18108, doi:10.1029/2009JD011867.
- Warren, L., J. A. Snoke, and D. E. James (2008), S wave velocity structure beneath the High Lava Plains, Oregon, from Rayleigh wave dispersion inversion, *Earth Planet. Sci. Lett.*, *274*, 121–131.
- Whipple, F. J. W. (1931), The investigation of air waves from explosions. Progress in England, *Q. J. R. Meteorol. Soc.*, *57*, 331–335.

C. de Groot-Hedlin, M. A. H. Hedlin, and K. Walker, Laboratory for Atmospheric Acoustics, Institute of Geophysics and Planetary Physics, Scripps Institution of Oceanography, University of California, San Diego, 9500 Gilman Dr., La Jolla, CA 92093, USA.

D. Drob, Upper Atmospheric Modeling Section, Naval Research Laboratory, 4555 Overlook Ave., Washington, DC 20375, USA.